



Mesoporous NiO nanomagnets as catalysts and separators of chemical agents

Mohamed Khairy^{a,b}, Sherif A. El-Safty^{a,b,*}, Mohamed Ismael^a, Hiroshi Kawarada^b

^a National Institute for Materials Science (NIMS), 1-2-1 Sengen, Tsukuba-shi, Ibaraki-ken 305-0047, Japan

^b Graduate School for Advanced Science and Engineering, Waseda University, 3-4-1 Okubo, Shinjuku-ku, Tokyo 169-8555, Japan

ARTICLE INFO

Article history:

Received 4 May 2012

Received in revised form 30 July 2012

Accepted 31 July 2012

Available online 10 August 2012

Keywords:

Mesoporous

Nickel oxide

Nanomagnet

Chemical oxidation

Organic pollutants

ABSTRACT

The development of a sustainable catalyst could potentially provide a long-term solution to industrial processes, especial those in the chemical industry, that require the production of a large quantity of raw materials manufactured from renewable resources. Therefore, establishing a proper design for a highly efficient and long-term reusable catalyst is one of the crucial environmental issues facing humanity. In this study, we developed a simple control for hierarchical mesoporous nickel oxide (NiO) nanomagnets (NMs) with flower- and sphere-like morphology and large mesopore cavities. In the fabrication of super-nanostructure NiO, features that were affected by the shape, surface, and size of particles exhibit high catalytic activities of chemical agents, such as *o*-aminophenol. Our findings show that the NiO NM with flower-like morphology NFs has higher catalytic activity toward the oxidation of organic contaminants than that of nanospheres NSs or even other magnetic nanoparticles (NPs) such as Fe₃O₄ NPs. Furthermore, the NiO NMs are capable of the high-gradient magnetic separation of organic contaminants from aquatic life with excellent reusability even after several cycles, which may help in wastewater management and supply. To understand the effectiveness of NiO NM functionalities in terms of hierarchical mesopore parameters, as well as in terms of shape- and size-morphologies in such chemical reactions, surface interaction and magnetic separation with chemical agents and theoretical calculations were performed.

© 2012 Elsevier B.V. All rights reserved.

1. Introduction

Hierarchically mesostructured transition metal oxide nanostructures are widely applied in a plethora of technologically important disciplines, ranging from catalysis [1–4], nano-engineering of surfaces [5], energy generation using fuel cells [6] and solar cells [7], optical imaging [8,9], phototherapy [10], and sensor applications [5–11]. Given that the catalytic activity of the transition metal crystals depends on the crystal face used and that different nanoparticles (NPs) with different shapes have different facets and different ratios of the number of atoms on corners and edges to those on the facets, catalysis is expectedly dependent on the NP shape used [12]. Considerable effort has been exerted to control the intrinsic nanostructure and morphology of these materials to achieve tunable properties. However, technical challenges, such as intensive and time-consuming synthetic conditions, remain.

With recent advancements in mesostructured materials and nanotechnology, new synthetic methods for effective nanocatalyst

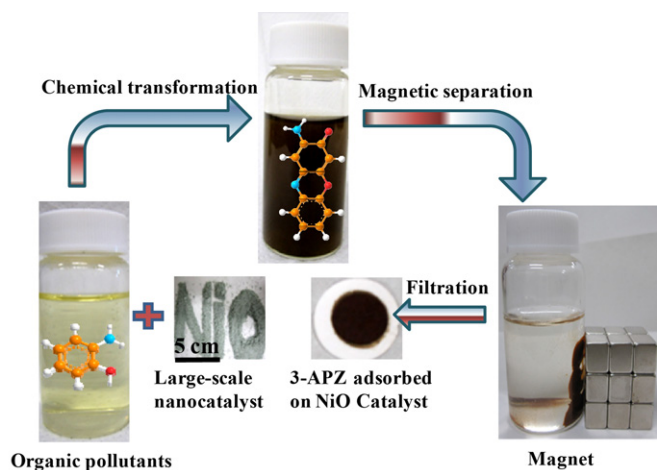
design have emerged. Template synthetic methods have been established as convenient approaches for the synthesis of mesoporous metal oxides. In these methods, either organic or inorganic particles could be used as sacrificial templates. However, the mesoporous structures tend to collapse during the removal of these templates at high temperature [13].

To date, nanoscale magnetic materials are considered to be potential adsorbents because of their large surface area and unique features of easy separation when subjected to external magnetic fields. These properties facilitate a wider range of applications, such as the purification of bio-molecules, magnetic refrigeration, magnetic resonance imaging enhancement, information storage, magneto-optical devices, solid devices, targeted drug delivery, cell separation, and environmental capture [14–17]. Magnetic NP features enable the easy recovery of catalysts in a liquid-phase reaction compared with cross-flow filtration and centrifugation, particularly when the catalysts are in the nanometer-size range and have high surface area that enables the creation of numerous catalytic sites for high activity levels.

Among the different magnetic NPs, nickel oxide (NiO) has received considerable attention for its unique magnetic properties, stability, and feasibility of preparation. NiO is a well-known wide band gap p-type semiconductor and antiferromagnetic material. The synthesis of NiO nanocrystals (NCs) with controlled but large-scale morphology are highly promising candidates because of their extensive applications as catalysts [1–4,18], lithium ion

* Corresponding author at: National Institute for Materials Science, 1-2-1 Sengen, Tsukuba, 305-0047 Japan; Graduate School for Advanced Science and Engineering, Waseda University, 3-4-1 Okubo, Shinjuku-ku, Tokyo 169-8555, Japan. Tel.: +81 298592135; fax: +81 298592025.

E-mail addresses: sherif@aoni.waseda.jp, sherif.elsafty@nims.go.jp (S.A. El-Safty).



Scheme 1. Catalytic transformation and removal of organic pollutants (3-APZ) using mesoporous NiO NM.

batteries and fuel cells [19], electrochromic display devices [20], optical gas sensors [21], magnetic materials [22], dye-sensitized photo-cathodes [23], and solar thermal absorbers [24]. Several NiO nanostructures with unique properties that are mainly affected by their size and morphology have recently been synthesized successfully, such as NiO nanoslices [25], nanoplates [25,27] and nanocolumns [25], nanorods [26–28], nanorings [28], nanosheets or nanoribbons [29], nanowires [30], nanotubes [31], and hollow nanospheres [32,33]. However, these synthetic strategies produce NiO with low porosity and magnetism. Thus, the development of a simple and feasible method for designing magnetic mesostructure NiO with controlled morphology is highly desirable and remains a great challenge to material scientists.

The petrochemical, chemical, and pharmaceutical industries produce wastewater that contains high concentrations of organic materials, which are extremely toxic to aquatic life. Given the increasing concern for public health and environmental quality, the transformation and complete removal of organic pollutants from the environment is imperative. Both functional processes are promising approaches for the treatment of organic contaminants to produce safe compounds, but present a great challenge to water suppliers. Aminophenols (APs) are widely used as reducing agents, as intermediates in chemical synthesis, bleaching, and hair dyes, and as materials for photography [34]. Therefore, the chemical oxidation and removal of APs from aquatic environments with an effective and sustainable global strategy has become a major public concern in almost all parts of the world. Recently, our group has reported on the fabrication of multidirectional porous mosaic-like NiO nanoplatelets using the hydrothermal strategy [35]. These porous NiO nanoplatelets showed an efficient chemical transformation of phenolic compounds. However, the treatment of organic contaminants is necessary to reduce storage space requirement and to prevent the release of such contaminants to the environment, which may cause long-term problems. To control the catalytic transformation and separation of chemical pollutants from the environment, the designing of nanomagnetic materials is highly desirable.

In this work, the hierarchical mesoporous NiO nanoflower (NF) and nanosphere (NS) magnets were fabricated using a simple and reproducible method. The mesoporous NiO nanomagnets (NMs) featured high mesopore porosity, surface area, and magnetization and can act as nanocatalysts with easy recovery and dynamic working ranges. In this regard, critical assessments for potential nanocatalyst design based NiO NMs in the chemical oxidation of phenolic pollutants are emphasized in this work. Our experimental

findings showed that the NiO NFs offer higher catalytic activity than NSs or even Fe_3O_4 NPs (Scheme 1). To understand the proposed chemical transformation mechanism of pollutants over NiO NMs, the energy profiles and the charge distribution of reactants and intermediates, as well as the magnetization effect on the resultant products, were examined using the density function theory (DFT). A major advantage of NiO NM catalysts is their retained texture, morphology, and magnetic characteristics (i.e., easy recovery) in terms of reactivity with fast chemical oxidation even after multiple cycles.

2. Experimental

All materials were of analytical grade and were used without further purification. Anhydrous nickel chloride, *o*-aminophenol (*o*-AP), sodium acetate (NaAc), and ethylene glycol (EG) were purchased from Japan Tokyo Chemical Industry Company Ltd. (Japan). The solutions of *o*-AP (0.015 mol L^{-1}) were prepared in water with 3% ethanol. The phenol concentration was $5 \times 10^{-4} \text{ mol L}^{-1}$ during the oxidation process.

2.1. Fabrication of mesoporous NiO NMs with flower-like morphology

The NiO NFs were synthesized using a one-pot hydrothermal method in the presence of EG and NaAc. During typical synthesis, 20 mmol of anhydrous nickel chloride precursor was dissolved in 40 mL of EG, followed by 40 mmol of anhydrous NaAc, which were then combined through sonication. The solution was loaded into a 100 mL Teflon-lined, stainless steel autoclave at 200°C for 8 h. The solution was then allowed to cool to room temperature. Finally, the precipitate was collected and washed ten times with distilled water and ethanol to remove the remaining agents, after which it was dried at 60°C .

2.2. Fabrication of magnetic NiO NSs

A combination of 1.47 g nickel chloride precursor and 4.5 g of anhydrous NaAc were dissolved in 25 mL Triethanol amine diluted in a 50 mL deionized H_2O plus 2.0 g polyethyleneimine. The solution was transferred to a 100 mL Teflon-lined, stainless steel autoclave, which was sealed and maintained at 200°C for 8 h and then cooled to room temperature. The precipitate was collected and washed ten times with distilled water and ethanol to remove the remaining agents and was then dried at 45°C . Finally, NiO powder was calcined at 270°C for 30 min with a heating of $2^\circ\text{C}/\text{min}$.

2.3. Catalytic reaction of mesoporous NiO NMs

The catalytic oxidation of phenolic compounds was conducted using NiO NMs as catalyst. The reaction was performed in water at varying temperatures ($25\text{--}40^\circ\text{C}$) using a thermostatic shaker at a constant shaking rate (150 rpm/min). In a typical kinetic experiment, the catalyst (0.025 g) solution is dissolved in 28 mL deionized water with shaking for 15 min and cleansing of N_2 gas at a specific temperature. ($25\text{--}40^\circ\text{C}$) Subsequently, 2 mL standard *o*-AP solution was added to the mixture for quick reduction, and the reaction time was recorded. The phenol concentration in the reaction vessel was $5 \times 10^{-4} \text{ M}$. At finite time, 3 mL of the solution was reduced and transferred to a quartz cell for measurement. The catalytic reaction was monitored spectrophotometrically at $\lambda = 430 \text{ nm}$ for 3-aminophenoxazone (3-APZ).

2.4. Materials characterization

N_2 adsorption/desorption isotherms at 77 K were used to investigate the textural surface properties and pore size distribution

with a BELSORP36 analyzer (JP. BEL Co., Ltd.). Prior to the adsorption/desorption process, all the samples were pre-treated at 200 °C for 8 h under vacuum until the pressure was equilibrated to 10^{-3} Torr. The specific surface area (S_{BET}) was calculated using the Brunauer–Emmett–Teller (BET) method with multipoint adsorption data from the linear segment of the N_2 adsorption isotherm. The pore size distribution was determined from the analysis of desorption branch of isotherm using the nonlocal density functional theory (NLDFT).

Small-angle X-ray scattering (SAXS) experiments were performed at room temperature. A two-dimensional (2D) confocal mirror (Rigaku Nanoviewer) and a pinhole collimator were used to obtain a focused high flux/high transmission; a monochromatic X-ray beam of Cu K α radiation ($\lambda = 1.54 \text{ \AA}$) was also used. The 2D SAXS patterns were recorded using a 2D detector (Bruker Hi-Star) covering a range of momentum transfer $q = (4\pi/\lambda) \sin(2\theta/2)$, from 0.2 to 10 cm^{-1} , where λ is the wavelength of the incident X-ray beam and 2θ is the scattering angle. The value of inter-particle distance (center-to-center) was calculated from $d = 2\pi/q_{\text{max}}$. Wide-angle powder X-ray diffraction (XRD) patterns were measured using an 18 kW diffractometer (Bruker D8 Advance) with monochromated Cu K α radiation. The sample measurement was repeated three times under rotation at various angles (15° , 30° , and 45°). The diffraction data were analyzed using the DIFRAC plus Evaluation Package (EVA) software with the PDF-2 Release 2009 databases provided by Bruker AXS. The standard diffraction data were identified according to the databases of the International Centre for Diffraction Data (ICDD). For poor quality diffraction data, the TOPAS package program provided by Bruker AXS 2009 for profile and structure analysis was applied to integrate various types of X-ray diffraction analyses by supporting all profile fit methods currently employed in powder diffractometry. X-ray photoelectron spectroscopy (XPS) was conducted using a PHI Quantera SXM (ULVAC-PHI) (PerkinElmer Co., USA) with monochromated Al K α radiation ($1.5 \times 0.1 \text{ mm}$, 15 kV, 50 W). The magnetic properties were measured with a Quantum Design MPMS superconducting quantum interferometer device (SQUID) with an applied magnetic field of up to 70 kOe.

The morphologies of the NiO samples were investigated via field emission scanning electron microscopy (FESEM, JEOL model 6500). Before insertion into the chamber, the NiO powders were ground and fixed onto a specimen stub using a double-sided carbon tape. Then, a 10 nm Pt film was coated via anion sputtering (Hitachi E-1030) at room temperature to obtain high-resolution micrographs. Before sputtering deposition, the Pt target (4 in. diameter, purity 99.95%) was sputter cleaned in pure Ar. The sputtering deposition system used for the experiments consists of a stainless steel chamber, evacuated down to 8×10^{-5} Pa with a turbo molecular pump backed up by a rotary pump. The Ar working pressure (2.8×10^{-1} Pa), the power supply (100 W), and the deposition rate were kept constant throughout these investigations. Moreover, to record the SEM micrographs of the Ni samples better, the scanning electron microscope was operated at 20 keV. High-resolution transmission electron microscopy (HRTEM), electron diffraction (ED), scanning transmission electron microscopy (STEM), and energy dispersive X-ray spectroscopy for elemental mapping (STEM-EDS) were performed using a JEOL JEM model 2100F microscope. HRTEM was conducted at an acceleration voltage of 200 kV to obtain a lattice resolution of 0.1 nm. The HRTEM micrographs were recorded using a CCD camera. STEM and STEM-EDS were carried out at a camera length of 80 cm and a spot size of 1 nm. In the HRTEM, ED, STEM, and STEM-EDS characterization, the NiO sample was dispersed in ethanol solution using an ultrasonic cleaner, and then dropped on a copper grid. Prior to inserting the samples into the HRTEM column, the grid was vacuum dried for 20 min.

The mass spectrometric experiments were recorded on a Micromass Platform quadrupole mass analyzer. APCI atmospheric pressure chemical ionization) spectra were recorded under operating conditions of: a capillary 3.5 kV, HV lens 0 kV, cone voltage 20 V, source temperature 150 °C, probe temperature 450 °C, ES eluent; 100% acetonitrile at 200 mL min^{-1} , nitrogen drying gas 250 L h^{-1} and APCI sheath gas 50 L h^{-1} . A Crison 501 pH meter was used and calibrated just before the measurements were recorded.

The absorbance spectrum of the heterogeneous catalytic reactions was recorded using a UV-vis spectrophotometer (Shimadzu 3150, Japan). Modeling calculations of the polymerization of 3-APZ product was done based on DFT calculations implemented in the Gaussian 03 suite program [36]. All calculations performed using an ordinary B3LYP functional theory, which comprises the hybrid Becke + Hartree–Fock exchange and Lee–Yang–Parr functional correlation with nonlocal corrections, were adopted with the basis set to 6-311++G(d,p). The solvent effects on the models were achieved using the polarized continuum model to obtain more reliable data.

3. Results and discussions

3.1. Design of mesoporous NiO NMs

Control over the particle morphology of NiO NMs was clearly made evident using one-pot, simple hydrothermal synthesis (Fig. 1). Field emission scanning electron microscopy (FE-SEM) micrographs revealed that NiO had a nanosized particle with an average diameter of ~ 300 and 500 nm for NiO NFs and NiO NSs, respectively. Generally, in the initial reaction period, acetate groups might coordinate with nickel to form nickel acetate precursors. The hydrolysis and/or alcoholysis of nickel acetate then occurred to form NiO nanomaterials. The possible formation mechanism of mesoporous NiO NMs with flower-like morphology involves two consecutive reactions, followed by orientation attachment and local Oswald ripening. Fig. 1(a and b) reveals that the crystal particles of NiO were aggregated in a petal-like manner and had smooth and fine surfaces aligned according to the flower morphology. On the other hand, the NiO NMs with sphere-like morphology was generated from the aggregation of NiO NPs (Fig. 1(c and d)). The magnified FE-SEM image of the NiO NMs showed that the morphological particles were either of shape- or size-controlled geometry, indicating the versatility of this method compared with the real control of the morphological and geometrical 3D NiO nanostructures.

Furthermore, evidence of the control formation of NiO NMs was revealed from the STEM image (Fig. 1(e and f)). The STEM image confirms the formation of the NiO NMs with an average size of 300 and 500 nm for NiO NFs and NiO NSs, respectively. The STEM-EDS mapping revealed the surface distribution of Ni, O, C, and Cl (Fig. 2). The STEM-EDS mapping indicates that Ni and O are uniformly distributed in the NF and NS surfaces. However, significant differences in the atomic distribution of Ni and O were evident. The elemental analysis of the NiO NMs by STEM-EDS indicates the presence of Ni, O, and C atoms. The O and Ni atoms were originally found in the NiO NCs, which had an [O]/[Ni] ratio of 0.79 and 0.71 for NFs and NSs, respectively. To estimate the surface composition of NiO NPs, XPS was performed. The surface atomic content of the NiO NFs was 50% for Ni 2p $_{3/2}$, 45% for O 1s, and 5% for C with an atomic ratio of ~ 0.9 , indicating the nickel overstoichiometry of NiO NPs on the surface. The results showed that the NMs comprised more nickel atoms and were deficient in oxygen atoms on the surface of NiO NPs. These values are consistent with STEM-EDS mapping analysis and are lower than the stoichiometric NiO because of the

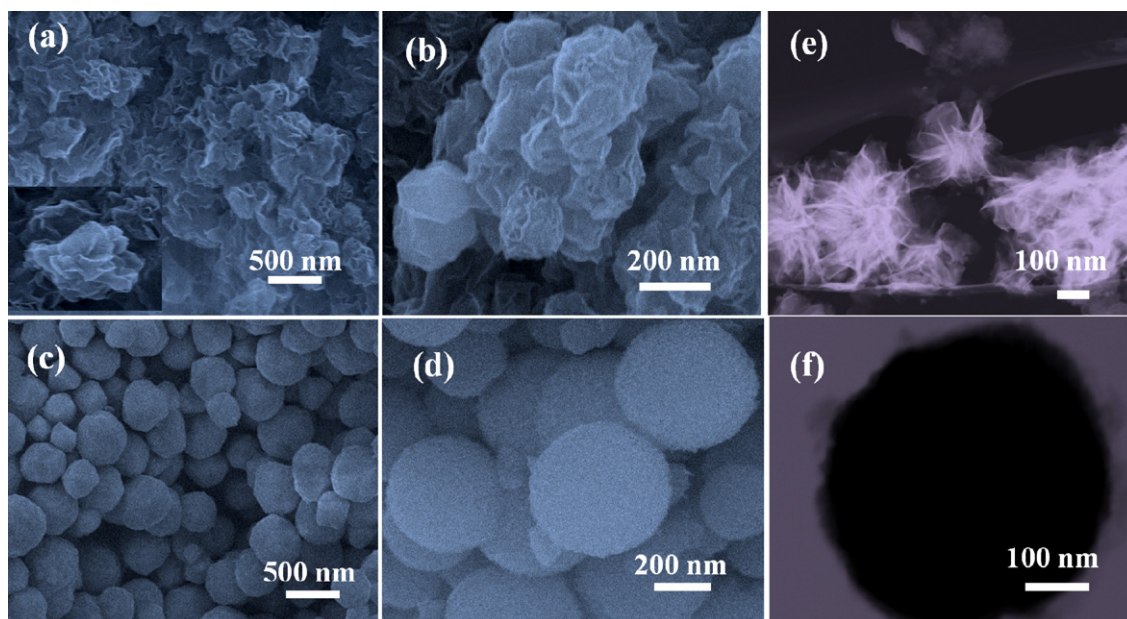


Fig. 1. FE-SEM and STEM images of NiO NMs (a, b, and e); mesoporous NiO NFs (c, d, and f); and mesoporous NiO NSs revealing the controlled size and shape of NiO NMs.

accession of Ni atoms. The characteristics of NiO NM surface architectures enhance the catalytic oxidation of organic contaminants or chemical agents. In addition, the altering of the surface composition for NiO NCs attributed to synthetic methodology is one of key factors to employ the uncompensated magnet moments, as previously reported by the Néel models [22].

The HRTEM images (Fig. 3) clearly indicate the controlling morphology of the NiO NMs (NFs and NSs) with an average size of ~300 and 500 nm, as well as disordered mesopore structures. These

HRTEM images of the NiO NFs (Fig. 3(a and b)) shows the formation of assembled petals with disordered pore surfaces. First, the NiO petals assembled to form NiO crystals with flower-like morphology. According to the distinct color contrast of TEM images associated with the flower structure, the nanopetals in the core region were observed to be more compact than those in the exterior. In addition, the aggregated petals are very thin; the thickness is less than 10 nm, as shown in Fig. 3(a). The most prominent feature was that the NFs showed uniform arrangements and continuous ordering of

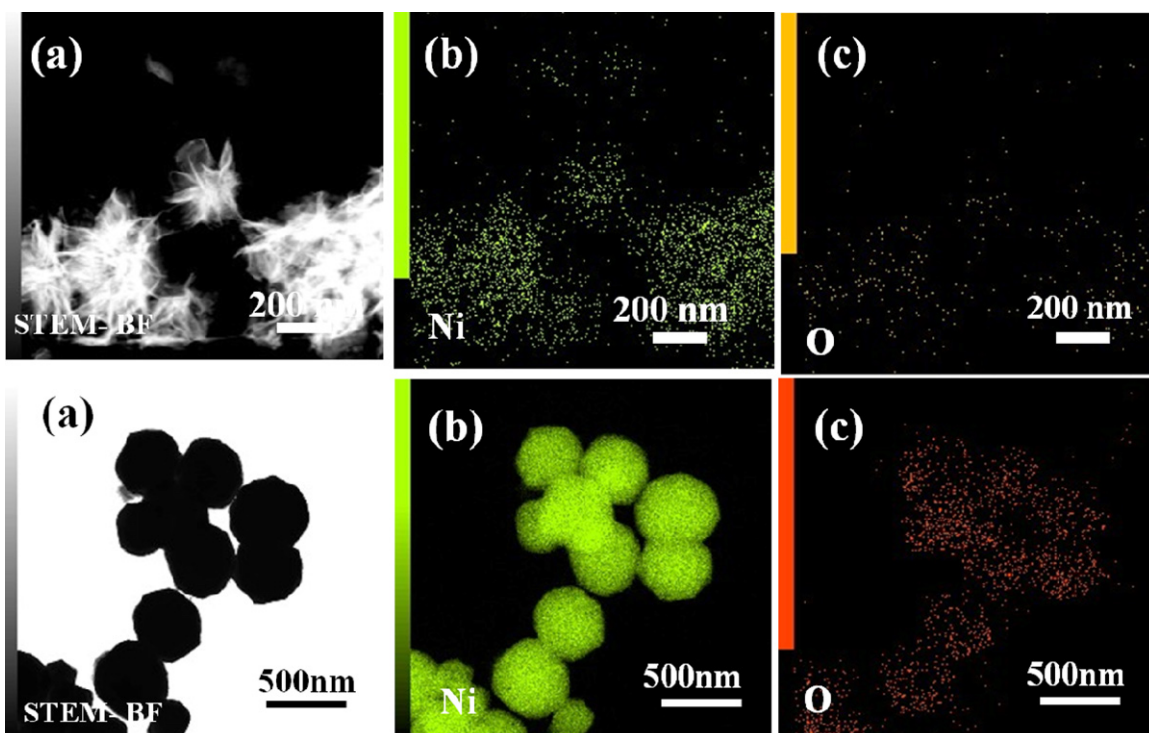


Fig. 2. STEM-EDS mapping of the mesoporous NiO NCs with flower- and sphere-like morphology; STEM images (a), nickel (b), and oxygen (c).

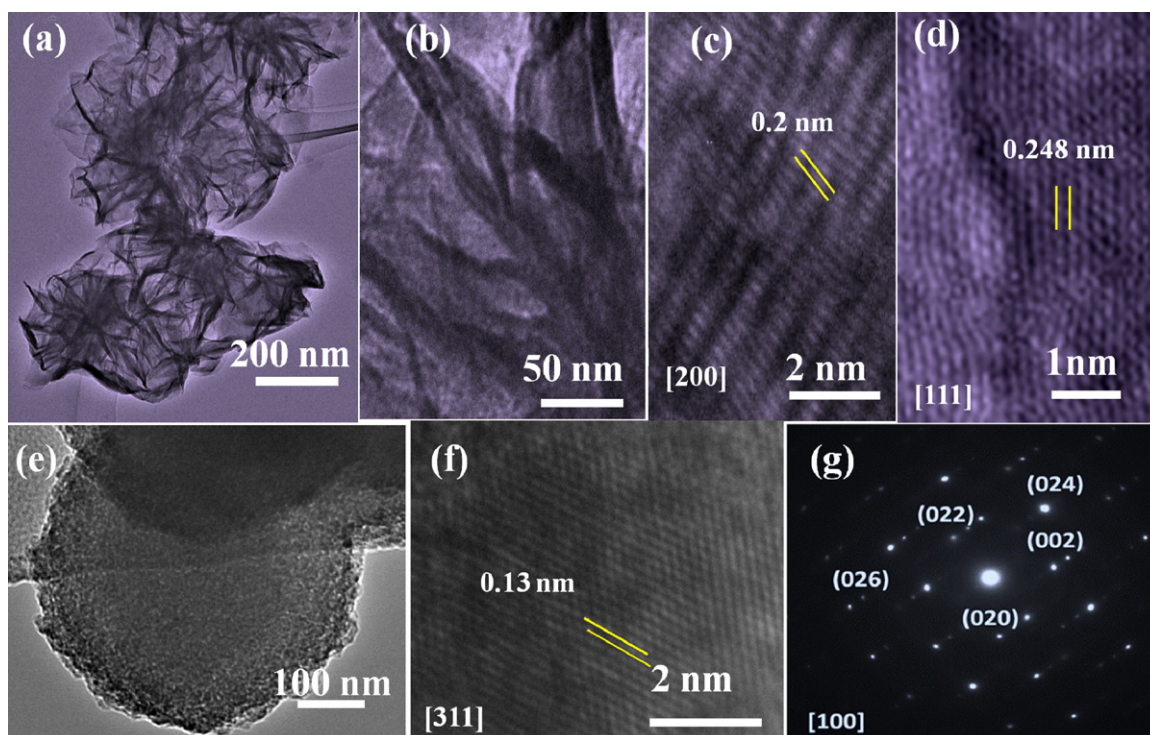


Fig. 3. Typical HRTEM images of NiO nanomagnet: (a) flower-like morphology with an average size of 300 nm, nanopetals at ~ 10 nm thick; (b–d) magnified view of the acicular branch; (e) HRTEM image NiO NS and magnified view of the crystal fringes; (f and g) corresponding ED pattern of selected areas revealing the high crystallinity of the NM.

lattice fringes over large-scale regions without distortion. Large-scale NC domains along the incidences are characteristic of an NiO cubic lattice.

The TEM micrographs (Fig. 3(c and d)) generally revealed well-organized lattice fringe arrays over a large area, with a distance between two lattice fringes being 0.2 and 0.248 nm featuring the interplanar space of (2 0 0) and (1 1 1) planes of cubic *Fm3m* crystal lattices. Fig. 3(e) shows the HRTEM image of the NS at 500 nm. The surface was not smooth because the spheres were formed from aggregated NCs. A higher magnification HRTEM image (Fig. 3(f)) shows that the lattice fringes had an interspacing of 0.13 nm, which corresponds to the distance between (3 1 1) planes of the cubic *Fm3m* NiO (JCPDS, No. 04-0835). The representative ED image (Fig. 3(g)) oriented with the preferable [1 0 0] incidence provided direct evidence of the formation of large-scale NC domains with cubic *Fm3m* symmetry. These results are consistent with the XRD results (see below).

3.2. Structural features of magnetic mesoporous NiO (NM) catalyst

The SAXS (Fig. 4(A)) profiles of the NiO NMs were subjected to absolute intensity scaling after normalizing the in-plane diffracted beams with substrate thickness. The scattering intensity and peak resolution were in the range of $1.3 < q < 2.2$, corresponding to $d_{(100)} = 3.6$ nm. Despite the broadening and low resolution in the intense scattering peak, the formation of mesostructures and the retention of the mesopore architectures inside the NiO NMs were evident [37]. Moreover, the wide angle XRD (inset, Fig. 4(a)) pattern exhibits typical diffraction peaks of cubic NiO phase (JCPDS, No. 04-0835).

The N_2 isotherms of the NiO NMs feature type IV isotherms with a H_2 -type hysteresis loop for typical mesocage materials with large pore cavities (10–30 nm) (Fig. 4(b)) [38]. This finding demonstrates

that our synthesis protocol enables effective control over the size and shape of the cage opening and cavity pores. Notably, the mesoporous NiO nanocatalysts featured a specific surface area of $S_{BET} = 119$ and $60.1 \text{ m}^2 \text{ g}^{-1}$ for NiO NFs and NSs, respectively. The pore size distribution of NiO NMs was calculated according to the NLDFT model (inset, Fig. 4(b)). Moreover, the NiO crystals with flower-like morphology exhibited a macroporous regime with an average value of 400 nm. The formation of the mesopore type is probably related to the pores present inside the nanopetals, which were formed between primary crystallites. In turn, the broad band and macroporous type may be related to the assembly of secondary petals to form flower architectures. Our findings showed that the NiO NFs had higher surface area than NiO NSs and that the NiO flowers were fabricated under sophisticated methods [33]. This result indicated that our method yields a high degree of mesopore orientation in the NiO NMs with high surface area and pore volume, which may enable the organic pollutant molecules to penetrate and be easily adsorbed onto the pore network matrices. Moreover, the magnetic characteristic of NiO NMs (Figs. 4 and 5) offers a large exposed surface area without the use of porous materials, which are often plagued by high mass transfer resistances [39].

3.3. Mesoporous NiO (NFs) magnetic characteristics

The magnetic hysteresis loop (M–H loop) of NiO NMs with flower- and sphere-like morphology measured at 300 K indicates magnetic properties, including saturation magnetization M_s and coercivity H_c . Although the NiO is an antiferromagnetic system, the fabrication of NiO nanostructures with large-scale NC domains and well-shaped morphologies exhibited new physical phenomena, such as weak ferromagnetism and paramagnetism. Such magnetic properties of NiO NF- and NS-like morphology might be attributed to the complicated spin configuration, as reported

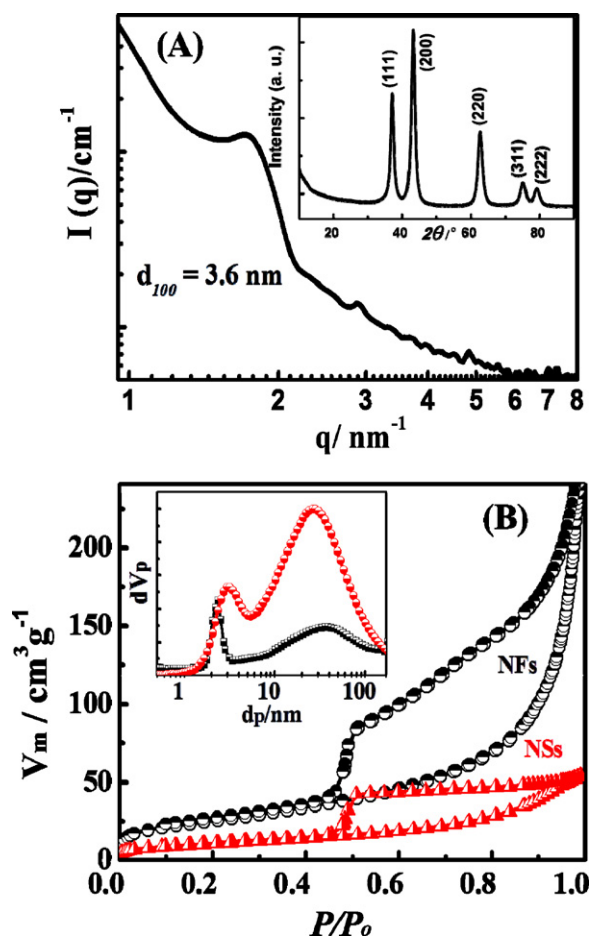


Fig. 4. (a) SAXS (inset: wide angle X-ray patterns) and (b) N_2 adsorption isotherm (inset: pore size distribution calculated by the NLDFT model of NiO nanomagnet with flower- and sphere-like morphology).

elsewhere [40]. Fig. 5 shows that the M_s values for the NiO NMs are 12.5 and 6.8 emu g^{-1} for NiO NFs and NSs, respectively. The results showed that the NiO NFs have higher paramagnetism than NiO NSs and other NiO nanomaterials reported previously [40,41]. The STEM (Fig. 2) and XPS (see Supplementary Fig. S1) results revealed that this paramagnetic behavior of NiO NFs and NSs might be attributed to the uncompensated Ni ions, which are most likely located at or close to the particle surfaces. The design of the NiO nanomagnetic catalysts facilitates the catalytic

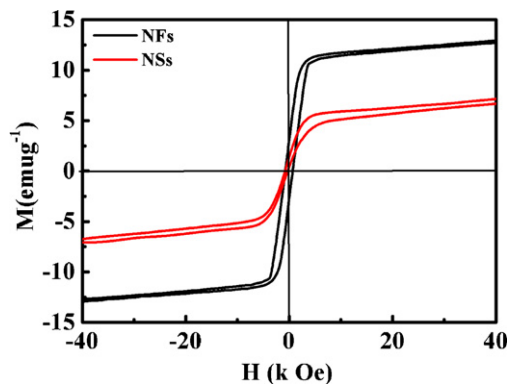


Fig. 5. Magnetic hysteresis loops of NiO-nanomagnet with flowers- and sphere-like morphology measured at 300 K.

transformation and separation of chemical pollutants from the environment.

3.4. NiO nanomagnetic catalysts

To investigate the magnetization, efficiency, and applicability of NiO NMs in the catalytic conversion and removal of organic contaminants using an external magnet, *o*-AP was used as a phenolic contaminate. The oxidation of *o*-AP was studied and monitored using UV-vis spectroscopy at $\lambda = 430$ nm in batch-contact experiments at a temperature range from 25 °C to 40 °C (Fig. 6). To support our work, the heterogeneous catalytic transformation reaction was conducted using a variety of magnetic materials, such as NiO and iron oxide nanoparticles. Our findings reveal that the transformation of *o*-AP in aquatic systems led to formation of nontoxic compounds (3-APZ), as reported recently [35]. To determine the molecular weight of the oxidation product through the catalytic conversion process, mass spectrometry was used (Fig. S2). The results showed that the *o*-AP oxidation product exhibited a molecular ion consistent with the formation of dimers ($C_{12}H_{11}N_2O_2$) [35]. These dimer ions are consistent with the protonated forms of the oxidation products of the *o*-AP, as shown in Scheme 2.

The physical characteristics of NiO nanomagnetic catalysts, such as particle morphology, large surface area, mesocage porosity, and magnetic properties, enabled the phenolic contaminants to access the active site of the NiO NMs. These unique characteristics of the NiO NMs enhanced not only the catalytic oxidation of organic pollutants to nontoxic chemical compounds, but also the removal of pollutants, as shown in Schemes 1 and 2. These results suggest that the magnetic feature did not have a significant effect on the catalytic reaction pathway and on the resultant product despite the significant recovery effect of chemical agents.

3.5. Kinetic and thermodynamic studies of magnetic catalysts

To understand the characteristics of the phenolic pollutant conversion process, the kinetics and thermodynamic parameters over NiO NMs were examined at varying temperature (25–40 °C) (Table 1). First-order and pseudo-second-order models were applied. Our findings indicate that the transformation of *o*-AP over NiO NMs was controlled by the first-order kinetics with respect to [phenol] molecules (Fig. 6(D)) as follows [35,38,39]:

$$\ln \left(\frac{A_{\infty}}{A_{\infty} - A_t} \right) = kmt \quad (1)$$

where A_{∞} is the absorbance of 3-APZ at infinite time; A_t denotes the absorbance of 3-APZ at time (t); k representing the first-order rate constant (s^{-1}), which is the only temperature-dependent parameter; m (g) is the amount of NiO nanocatalyst in grams. The heterogeneous rate constant (k) of the transformation reaction increased with increasing temperatures (Fig. 6(D)). The key achievement in this catalytic NM study is that the NiO NFs catalysts significantly showed doubled catalytic efficiency in terms of the rate constant and degree of conversion (Fig. 6) compared with NiO NS catalysts. This finding indicates the unique characteristics of NiO NF catalysts, such as morphology, large surface area, and high porosity, which serve as a key parameter in enhancing the accessibility of the active sites to the phenolic contaminants. From the value of the heterogeneous rate constant, the Gibbs free energy change, E_a^\ddagger , ΔG^\ddagger , ΔH^\ddagger , and ΔS^\ddagger values can be derived using the Arrhenius and Eyring equations. The ΔH^\ddagger activation value and the ΔG^\ddagger values were in the range of the chemical reaction control.

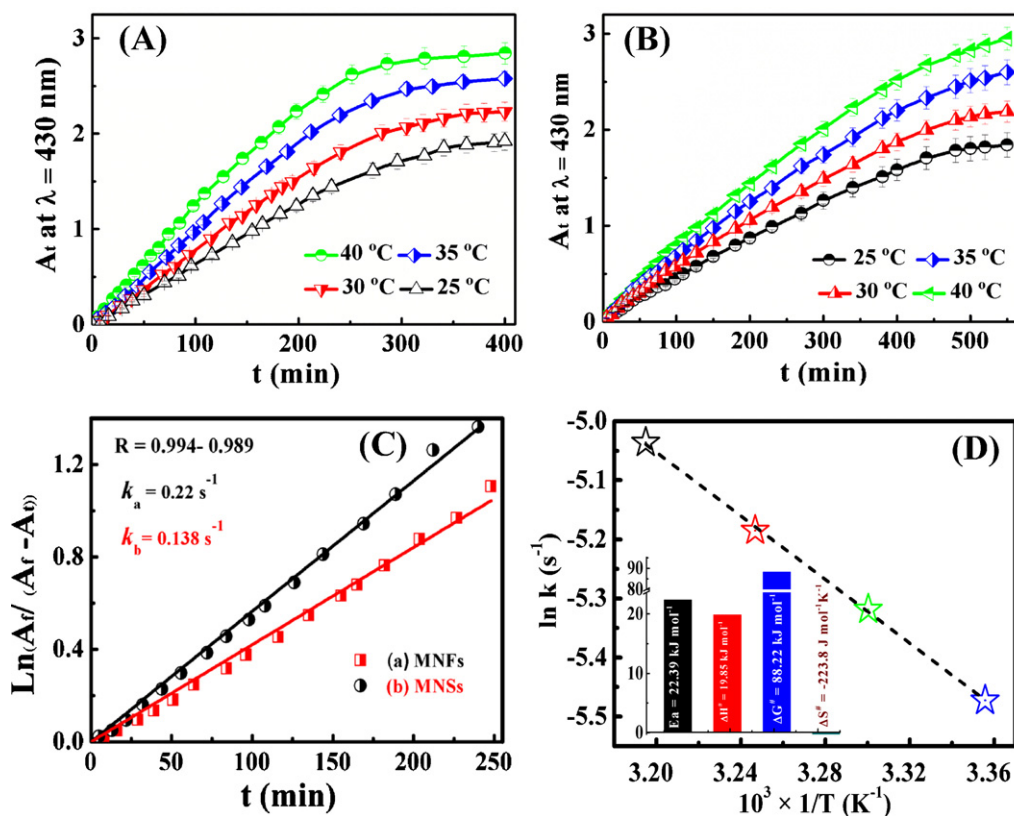


Fig. 6. The effect of various reaction temperatures on the time-rate dependence of 3-APZ formation at 430 nm over NiO NFs (A) and NiO NSs (B). The integrated first-order reaction rate of the transformation of *o*-AP to 3-APZ at NiO NMs at 25 °C (C) and the corresponding kinetic parameters during the transformation reaction over NiO NFs (D). Note that the concentration of *o*-AP was 5×10^{-4} M.

The thermodynamic parameters were derived from the van't Hoff equation. The plot of $\ln K_c$ vs. $1/T$ gives the numerical values of ΔH , ΔG , and ΔS using the following relations (Table 1):

$$\Delta G = -RT \ln K_c \quad (2)$$

$$\ln K_c = \frac{-\Delta H}{RT} + \frac{\Delta S}{R} \quad (3)$$

where ΔH , ΔG , and ΔS , and T are the change in enthalpy, change in entropy, change in Gibbs free energy, and temperature in K, respectively. R is the gas constant, and K_c is equilibrium constant [38,43]. Despite the magnetization effect of NiO catalysts, the transformation reaction of *o*-AP was spontaneous and more favorable at high temperatures, resulting in an endothermic process with a positive value of ΔH , as reported in NiO nanoplatelet catalysts. This finding indicated that the increase in reaction temperature facilitated the diffusion through the NiO NM pores (Table 1, and Fig. 6(C)). Furthermore, the NiO NFs provided high accessibility. The mobility of the small molecules of the phenolic pollutants, such as *o*-AP (approximately 6 Å) was significantly affected by the degree of porosity and exposed surface area (Fig. 6(D)). The thermodynamic and kinetic

parameters (Table 1) during the course of chemical transformation generally indicated the migration and effective transformation of pollutants through the interior of mesoporous cavities of the NiO NM.

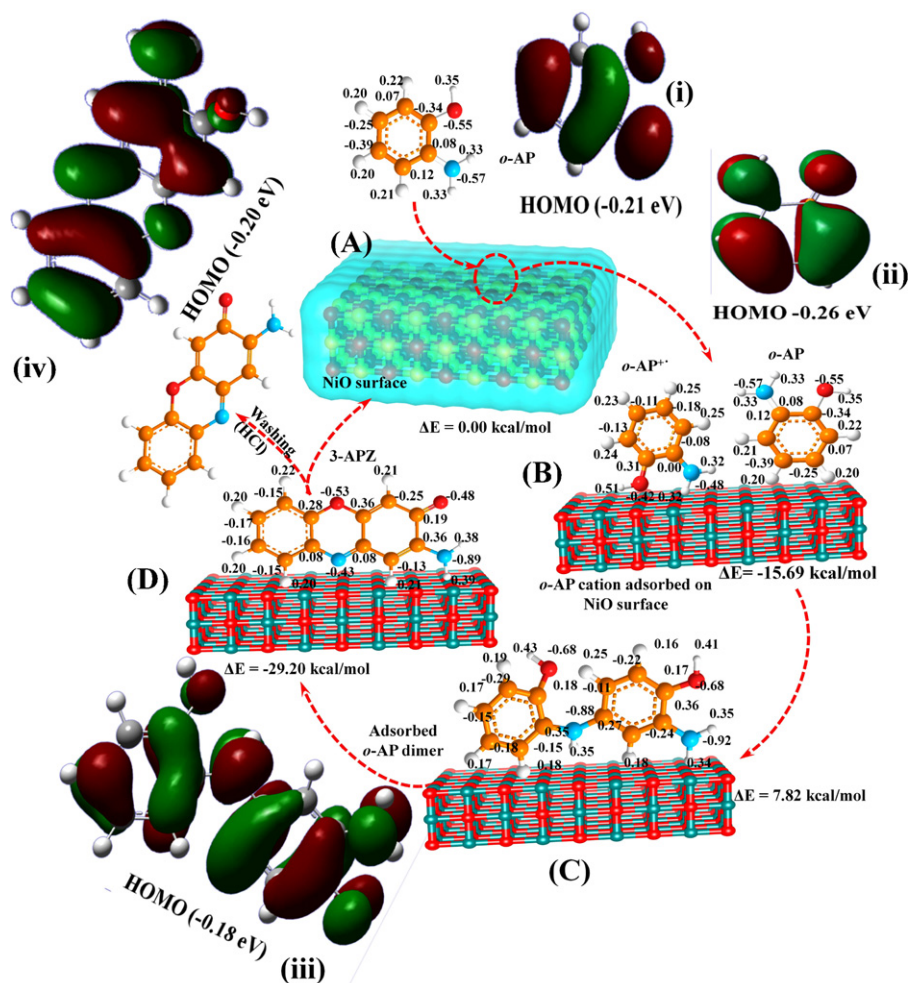
3.6. Catalytic mechanism of *o*-AP over NiO NMs

To study the feasibility of using NiO NM catalysts in high-performance chemical transformation, the catalytic transformation mechanism was investigated using the DFT [36]. These calculations provide details to facilitate further understanding of the complex heterogeneous catalytic reaction in terms of reactant–solid NP binding and intermediate formation. Evidently, the geometric orientation of the functional groups $-\text{NH}_2$ and $-\text{OH}$ is very important in the heterogeneous catalytic reaction network of phenolic pollutants. Scheme 2 shows the structures and charge distribution of the *o*-AP molecule and its oxidation product. The highest electronegativity allocated on the *o*-AP amino group was -0.59 , which suggests that the oxidation is initiated through electron loss from the amino group. Subsequently, the produced cation attacked the aromatic

Table 1

Kinetic and thermodynamic features; heterogeneous reaction rate constant of the NiO nanomagnet during oxidation of $[5 \times 10^{-4} \text{ M}]$ *o*-APs at different temperatures. (Note: E_a , ΔH , ΔS and ΔG are the energy of activation, enthalpy, entropy, and free Energy, respectively.).

Kinetic parameters						Thermodynamic parameters			
T (°C)	$10^3 k$ (s ⁻¹)	E_a (kJ mol ⁻¹)	ΔH^\ddagger (kJ mol ⁻¹)	ΔS^\ddagger (J mol ⁻¹ K ⁻¹)	ΔG^\ddagger (kJ mol ⁻¹)	K_c	ΔH (kJ mol ⁻¹)	ΔS (J mol ⁻¹ K ⁻¹)	ΔG (kJ mol ⁻¹)
25	4.2				86.54	0.97			0.157
30	4.9				87.66	1.03			-0.241
35	5.6	22.39	19.85	-223.8	88.78	1.31	23.9	79.7	-0.64
40	6.5				89.89	1.50			-1.039



Scheme 2. Expected transformation mechanism: (a) *o*-AP molecules diffused to NiO surface; (b) formation of radical at the surface; (c) formation of dimer; and (d) adsorption of 3-APZ onto the magnetic NiO surface. (i–iv) highest occupied molecular orbital (HOMO) with respect to the transformation mechanism.

ring of another *o*-AP molecule in the *p*-position with respect to the –OH group, which is the most electronegative part of the aromatic ring (–0.39 for *o*-AP) (Fig. S3). Notably, the HOMO–LUMO band gap was very small, suggesting that the *o*-AP has a tendency toward further polymerization (see Scheme 2, Supplementary Fig. S4). Our findings generally revealed that the surface of NiO NMs enhanced the catalytic reaction by ~10 kcal/mol. Indeed, this theoretical study provides evidence of the feasibility of our catalyst in high chemical oxidation processes. Moreover, the adsorption energy (which reflects the catalytic activity) calculation provides first insight into the role of the electronic structure of NiO on the surface activity.

3.7. NiO NM catalysts for separation of chemical agents

Magnetic NPs with good stability have unique properties that are of great interest in catalysis, mainly in biotechnology and biomedicine applications. Such magnetic NPs might be effective separators and collectors of catalysts, waste, biochemical products, and cells [2–4]. To demonstrate the applicability of mesoporous NiO NMs in the efficient chemical oxidation and separation of organic contaminants, the heterogeneous catalytic reaction of *o*-AP was performed using a variety of non-magnetic materials that were previously fabricated (see Supplementary Fig. S5) [40–43]. The results revealed that mesoporous NiO NFs have higher catalytic efficiency of chemical agents than NiO NSs and small NiO NPs

or even super-paramagnetic Fe₃O₄ NPs. The morphology, surface composition, and parameters (high S_{BET} and pore volume uniform porosity) of the mesoporous NiO NFs play a role in achieving not only a high degree of pollutant conversion into nontoxic chemicals, but also a high-gradient magnetic separation of organic contaminants (Scheme 1).

3.8. Applicability and structural features of NiO nanomagnet after recycling

A major advantage of NiO NM catalysts is their retained texture, morphology, and magnetic characteristics in terms of reactivity with fast chemical transformation even after multiple cycles. Although the improvement in the reducibility and reversibility of the catalyst is a challenge, NiO NMs can extend the control of the oxidative transformation and separation of phenolic pollutants from wastewater even after several cycles (Fig. 7(a)). However, after the first set of reaction experiments, the NiO nanocatalysts were collected and washed several times with a mixed solution of HCl (1 mM) and ethanol in air to remove the adsorbance product on the surfaces and were then dried overnight at 100 °C. The results showed that the NiO NF catalysts lost approximately 6% of their original efficiency after the fourth cycle. This finding indicates that the binding of organic moieties (reactant and product) onto the NiO catalyst did not result in the deformation of the internal- and external-ordered mesoporous surface sites (Fig. 7(b and d)).

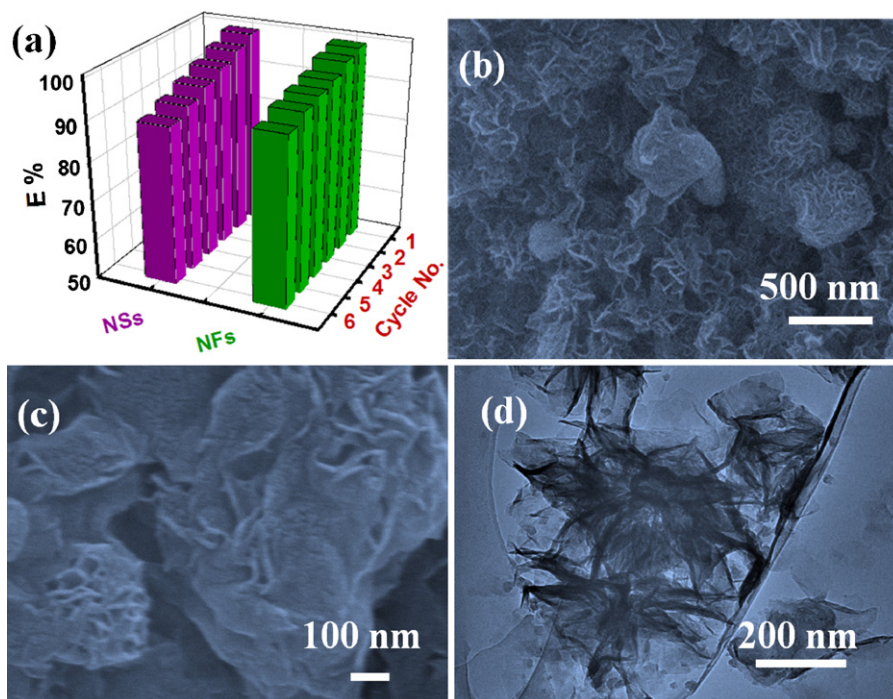


Fig. 7. (a) Catalytic efficiency (E%) of the NiO NMs after multiple cycles at 25 °C. [E% of the NiO NMs was calculated from the % ratio of the reaction rate constant (k/s^{-1}) per recycle (No.) and the rate constant obtained from the initial use of the catalysts; the FE-SEM (b–c) and TEM (d) micrographs of mesoporous NiO NM after the third cycle.

Such long-term reversibility renders the mesoporous NiO NMs catalyst applicable for further oxidative transformation and removal processes [42].

4. Conclusion

We developed a simple and feasible method for the design of magnetic mesoporous NiO NCs with flower- and sphere-like morphology without using hard or soft templates. These large-scale mesoporous NiO NMs with controlled morphology are highly promising candidates in the catalytic transformation of phenolic pollutants (such as *o*-AP). The key features of magnetic NiO NMs include high catalytic activity and reusability. Moreover, the magnetic property of NiO NMs does not affect the catalytic reaction pathway. To understand the proposed chemical oxidation mechanism of phenolic pollutants, the energy profiles and charge distribution of reactants, intermediates, and products were calculated using the DFT. A major advantage of NiO nanocatalysts is their retained texture, morphology, and magnetic characteristics in terms of reactivity with fast chemical transformation even after multiple cycles. We expect these mesoporous NiO NMs to be a promising development for nanoscale devices. Moreover, this study may provide guidelines for magnetic NP optimization for use in effective chemical and biochemical processing applications, particularly in the field of catalysis and environmental clean-up systems, for the transformation and removal of organic pollutants from wastewater.

Appendix A. Supplementary data

Supplementary data associated with this article can be found, in the online version, at <http://dx.doi.org/10.1016/j.apcatb.2012.07.036>.

References

- [1] A.T. Bell, *Science* 299 (2003) 1688–1690.
- [2] Y. Wang, A. Zhu, Y. Zhang, C.T. Au, X. Yang, *Applied Catalysis B: Environmental* 81 (2008) 141–149.
- [3] H.J. Gallon, X. Tu, M.V. Twigg, J.C. Whitehead, *Applied Catalysis B: Environmental* 106 (2011) 616–620.
- [4] A. Chen, P. Holt-Hindle, *Chemical Reviews* 110 (2010) 3767–3804.
- [5] A.N. Shipway, E. Katz, I. Willner, *ChemPhysChem* 1 (2000) 18; S.A. El-Safty, M. Khairy, M. Ismael, *Sensors and Actuators B* 166 (2012) 253–263; S.A. El-Safty, M.A. Shenashen, M. Khairy, M. Ismael, *Chemical Communications* 48 (2012) 6708–6710; S.A. El-Safty, M.A. Shenashen, M. Khairy, M. Ismael, *Advanced Functional Materials* (2012), doi:10.1002/adfm.201200393.
- [6] Y.H. Lin, X.L. Cui, C. Yen, C.M. Wai, *Journal of Physical Chemistry B* 109 (2005) 14410–14415.
- [7] S. Nakade, Y. Saito, W. Kubo, T. Kitamura, Y. Wada, S.I. Yanagida, *Journal of Physical Chemistry B* 107 (2003) 8607–8611.
- [8] Y. Jin, C. Jia, S.W. Huang, M.O. Donnell, X. Gao, *Nature Communications* 1 (2010) 41.
- [9] N. Liu, M. Tang, M. Hentschel, H. Giessen, A.P. Alivisatos, *Nature Materials* 10 (2011) 31–636.
- [10] T.L. Lai, C.C. Lee, G.L. Huang, Y.Y. Shu, C.B. Wang, *Applied Catalysis B: Environmental* 78 (2008) 151; D.K. Kirui, D.A. Rey, C.A. Batt, *Nanotechnology* 21 (2010) 105.
- [11] T. Balaji, S.A. El-Safty, H. Matsunaga, T. Hanaoka, F. Mizukami, *Angewandte Chemie International Edition* 45 (2006) 7202–7208.
- [12] R. Narayanan, M.A. El-Sayed, *Journal of the American Chemical Society* 126 (2004) 7194–7195.
- [13] K. Butter, K. Kassapidou, G.J. Vroege, A.P. Philipse, *Journal of Colloid and Interface Science* 287 (2005) 485–495.
- [14] Y. Kobayashi, M. Horie, M. Konno, B.R. González, M.L. Liz-Marzán, *Journal of Physical Chemistry B* 107 (2003) 7420–7425.
- [15] M. Mikhaylova, D. Kim, N. Bobrysheva, M. Osmolowsky, V. Semenov, T. Tsakalakos, M. Muhammed, *Langmuir* 20 (2004) 2472.
- [16] Z.L. Liu, X. Wang, G.H. Du, Q.H. Lu, Z.H. Ding, J. Tao, *Journal of Materials Science* 39 (2004) 2633.
- [17] S. Xuan, F. Wang, X. Gong, S.K. Kong, J.C. Yua, K.C-F. Leung, *Chemical Communications* 47 (2011) 2514–2516.
- [18] Y. Li, B.C. Zhang, X.W. Xie, J.L. Liu, Y.D. Xu, W.J. Shen, *Journal of Catalysis* 238 (2006) 412.
- [19] P. Poizat, S. Laruelle, S. Grugeon, L. Dupont, J.M. Tarascon, *Nature* 407 (2000) 496.
- [20] M.C.A. Fantini, F.F. Ferreira, A. Gorenstein, *Solid State Ionics* 152 (2002) 867–872.
- [21] G. Mattei, P. Mazzoldi, M.L. Post, D. Buso, M. Guglielmi, A. Martucci, *Advanced Materials* 19 (2007) 561.
- [22] S.D. Tiwari, K.P. Rajeev, *Thin Solid Films* 505 (2006) 113.
- [23] A. Nattestad, M. Ferguson, R. Kerr, Y.B. Cheng, U. Bach, *Nanotechnology* 19 (2008) 295304.
- [24] J.G. Cook, F.P. Koffyberg, *Solar Energy Materials* 10 (1984) 55–67.

- [25] X. Zhang, W. Shi, J. Zhu, W. Zhao, J. Ma, S. Mhaisalkar, T.L. Maria, Y. Yang, H. Zhang, H.H. Hang, Q. Yan, *Nano Research* 3 (2010) 643–652.
- [26] N. Cordente, M. Respaud, F. Senocq, M.J. Casanove, C. Amiens, B. Chaudre, *Nano Letters* 1 (2001) 565.
- [27] X. Wang, L. Li, Y.G. Zhang, S.T. Wang, Z.D. Zhang, L.F. Fei, Y.T. Qian, *Crystal Growth and Design* 6 (2006) 2163.
- [28] J. Liang, Y.D. Li, *Chemistry Letters* 32 (2003) 1126.
- [29] Z.H. Liang, Y.J. Zhu, X.L. Hu, *Journal of Physical Chemistry B* 108 (2004) 3488.
- [30] Z.Y. Wu, C.M. Liu, L. Guo, R. Hu, M.I. Abbas, T.D. Hu, H.B. Xu, *Journal of Physical Chemistry B* 109 (2005) 2512.
- [31] G. Malandrino, L.M.S. Perdicaro, I.L. Fragala, R.L. Nigro, M. Losurdo, G. Bruno, *Journal of Physical Chemistry C* 111 (2007) 3211.
- [32] X.B. Chen, S.S. Mao, *Chemical Research* 107 (2007) 2891.
- [33] B. Zhao, X.-K. Ke, J.-H. Bao, C.-L. Wang, L. Dong, Y.W. Chen, H.-L. Chen, *Journal of Physical Chemistry C* 113 (2009) 14440–14447.
- [34] J. Kaizera, R. Csonkab, G. Speier, *Journal of Molecular Catalysis A: Chemical* 1 (2002) 91–96.
- [35] M. Khairy, S.A. El-Safty, M. Ismael, H. Kwarada, *Applied Catalysis B: Environmental* 123 (2012) 162–173.
- [36] M.J. Frisch, et al., *Gaussian 03*, in: Revision D. 01, Gaussian, Inc., Wallingford, CT, 2004.
- [37] N.D. Hoa, S.A. El-Safty, *Nanotechnology* 22 (2011) 485503.
- [38] K.S.W. Sing, D.H. Everett, R.A.W. Haul, L. Moscou, R.A. Pierotti, J. Rouquerol, T. Siemieniewska, *Pure Applied Chemistry* 57 (1985) 603–619; S.A. El-Safty, Y. Kiyozumi, T. Hanaoka, F. Mizukami, *Applied Catalysis B: Environmental* 82 (2008) 169–179; S.A. El-Safty, Y. Kiyozumi, T. Hanaoka, F. Mizukami, *Applied Catalysis A: General* 337 (2008) 121–129.
- [39] G.D. Moeser, K.A. Roach, W.H. Green, T.A. Hatton, P.E. Laibinis, *AIChE Journal* 50 (2004) 2835–2848.
- [40] M.Y. Ge, L.Y. Han, U. Wiedwald, X.B. Xu, C. Wang, K. Kuepper, P. Ziemann, J.Z. Jiang, *Nanotechnology* 21 (2010) 425702; S.A. El-Safty, A. Shahat, Md.R. Awual, *Journal of Colloid and Interface Science* 359 (2011) 9–18.
- [41] M.P. Proenca, C.T. Sousa, A.M. Pereira, P.B. Tavares, J. Ventura, M. Vazquez, J.P. Araujo, *Physical Chemistry Chemical Physics* 13 (2011) 9561–9567.
- [42] X. Chen, L. Li, X. Sun, Y. Liu, B. Luo, C. Wang, Y. Bao, H. Xu, H. Peng, *Angewandte Chemie International Edition* 50 (2011) 1–5.
- [43] N. Nasuha, B.H. Hameed, *Chemical Engineering Journal* 166 (2011) 783–786.